

Laser-Driven Calorimetry and Chemometric Quantification of Standard Reference Material Diesel/Biodiesel Fuel Blends

Werickson Fortunato de Carvalho Rocha^a, Cary Presser^{b*}, Shannon Bernier^c, Ashot Nazarian^d, David A. Sheen^b

^aNIST Associate, National Institute of Metrology, Quality and Technology (Inmetro), 25250-020 Duque de Caxias, RJ, Brazil

^bMaterial Measurement Laboratory, National Institute of Standards and Technology, Gaithersburg, MD 20899, USA

NIST SURF Student^c, NIST Associate^d, Material Measurement Laboratory, National Institute of Standards and Technology, Gaithersburg, MD 20899, USA

Abstract

Requirements for blends of drop-in petroleum/bio-derived fuels with specific thermophysical and thermochemical properties highlights the need for chemometric models that can predict these properties. Multivariate calibration methods were evaluated using the measured thermograms (i.e., change in temperature with time) of 11 diesel/biodiesel fuel blends (including four repeated runs for each fuel blend). Two National Institute of Standards and Technology Standard Reference Material[®] (SRM[®]) pure fuels were blended by serial dilution to produce fuels having diesel/biodiesel volumetric fractions between (0 to 100) %. The fuels were evaluated for the prepared fuel-blend volume fraction and total specific energy release (heating value), using a laser-driven calorimetry technique, termed 'laser-driven thermal reactor'. The experimental apparatus consists of a copper sphere-shaped reactor (mounted at the center of a stainless-steel chamber) that is heated by a high-power continuous wave Nd:YAG laser. Prior to heating by the laser, liquid sample is injected onto a copper pan substrate that rests near the center of the reactor and is in contact with a fine-wire thermocouple. A second thermocouple is in contact with the sphere-reactor inner surface. The thermograms are then used to evaluate for the thermochemical characteristic of interest.

Partial least squares (PLS) and support vector machine (SVM) models were constructed and evaluated for SRM-fuel-blend quantification, and determination of prepared fuel-blend volume fraction and heating value. Quantification of the fuel-blend thermograms by the SVM method was found to better correlate with the experimental results than PLS. The combination of laser-driven calorimetry and multivariate calibration methods has demonstrated the potential application of using thermograms for fuels quantification and analysis of fuel-blend properties.

Keywords

Chemometric analysis, chemometric quantification, diesel fuel blends, laser-driven calorimetry, multivariate calibration methods, standard reference materials

***Corresponding Author**

Cary Presser
Research Engineer
Chemical Sciences Division
Material Measurement Laboratory

Mailing Address:

National Institute of Standards and Technology
Bldg. 221, Rm. B310
100 Bureau Dr., Stop 8320
Gaithersburg, MD 20899-8320

Contact Information:

301-975-2612 (tel)
cpresser@nist.gov (email)

1. Introduction

The development and use of alternative bio-derived fuels for transportation and propulsion is of importance since these sources of energy are renewable, virtually unlimited, reduce the national dependency on foreign fossil supplies, and reduce hydrocarbon and carbon dioxide emissions into the atmosphere. To ensure biofuel commercialization into the U.S. marketplace, and competitiveness with international competitors, biofuel standard materials (based on well-characterized reference biofuel compositions) must be available that are characterized not only for their physical and chemical properties, but also for their thermochemical behavior. Knowledge of the thermochemical behavior defines how temperature effects fuel heat transfer and reactivity. The fuel thermal character is especially important for blending of petroleum-based with bio-derived fuels because petroleum-fuel industries must be assured that drop-in biofuel replacements will maintain current engine performance and reduce emission levels. Thus, use of screening methodologies, based on both experimental and statistical evaluations, would assist industry in rationally reducing the number of biofuel candidates, so that resources could be directed toward testing in full-scale platforms. Experimental evaluations for fuel selection and combustion performance in engines have progressed such that merit functions are defined to better understand fuel and engine interactions [1]. Statistical evaluations have also been used to provide well-controlled blend composition for meeting fuel-quality specifications prior to testing [2]. The requirement for specific fuel thermophysical and thermochemical properties emphasizes the need to build chemometric models for predicting these properties.

The use of blending certified reference materials to make an in-lab standard of essentially arbitrary properties is a well-established practice [3]. A range of analytical techniques has been used along with chemometric methodologies to compare and quantify such fuel blends, and in particular for biodiesel fuels [4-13]. For example, Alves and Poppi [14] describes the use of near-infrared spectroscopy to develop multivariate calibration models for determining biodiesel content in diesel fuel blends while controlling physicochemical characteristics. Support vector machine models were found to provide better results than partial least squares models in that they provided the required accuracy in reporting biodiesel content, required minimal data preprocessing, and were selective for biodiesel (being unaffected by other mixture components). Oliveira et al. [15] used near-infrared spectroscopy to monitor the quality of biodiesel and petrodiesel fuel blends. Chemometric approaches were used to identify diesel fuel samples that were out of specification relative to the biodiesel content (i.e., due to biodiesel contamination with vegetable oil and diesel fuel contamination with naphtha). Other authors have studied petrodiesel fuels for quality-control purposes, based on chromatography [16, 17], infrared spectroscopy [18-24], Fourier transform infrared spectroscopy [25], ¹H-nuclear-magnetic-resonance spectroscopy [26-28], Raman spectroscopy [29-32], and laser calorimetry [33, 34]. Although most of these chemometric investigations have focused on modeling blend quality, based on chemical composition and physicochemical characteristics, these models should also consider the effects of thermochemical characteristics on blend quality. In this investigation, chemometric models were used to quantify the heating value for a range of

diesel/biodiesel blend compositions and determine if such models could be a useful tool to screen fuels for further testing.

1.1 Laser-driven calorimetry

In this investigation, we focus on applying chemometric approaches to determine the suitability of using a developing calorimetry technique, the laser-driven thermal reactor (LDTR) [35]. The experimental apparatus consists of a copper sphere-shaped reactor (mounted at the center of a stainless-steel chamber) that is heated by a high-power continuous wave Nd:YAG laser. Prior to heating by the laser, liquid sample is injected onto a copper pan that rests near the center of the reactor and is in contact with a fine-wire thermocouple. The change in temperature with time ('thermogram') is measured by the thermocouple and evaluated for the thermochemical characteristic of interest. Derivative profiles are also defined from the thermograms to highlight the thermogram features. Due to preferential vaporization of the different fuel components, the thermogram should be unique for a given blend. The advantage of this technique is that, unlike other commercial thermal analysis techniques (differential scanning calorimetry, thermogravimetric analysis, bomb calorimetry, etc.), the LDTR accounts for the total thermal response of a substance due to the heat exchanged with the surroundings by both thermal and chemical mechanisms (see [36]). As a result, the system is designed to heat substances at heating rates appropriate for capturing the temporal thermal behavior (i.e., exothermic, endothermic response) during fuel chemical decomposition and reaction, and thereby allow calculation of the thermochemical characteristics (e.g., specific energy release rate and total specific energy release). Other benefits are that the LDTR: 1) uses smaller sample sizes with higher heating rates than achievable with commercially available systems with sample heating over a period of minutes instead of hours, and 2) preserves the original sample physical characteristics prior to a measurement run. Comparison of LDTR and thermogravimetric analysis measurements is available in Presser and Nazarian [36]. The LDTR has been applied to multicomponent and multiphase solid and liquid substances, such as with conventional and biodiesel fuels [36-38].

1.2 Regression models: Partial least squares and support vector machines

Partial least squares (PLS) is a multivariate calibration method for modeling the relationship between two data matrices X and Y . The matrix X has information contained in the dataset (independent variables), in this case, the LDTR thermogram parameters (i.e., time and sample temperature), and Y has the responses (dependent variables or 'predictors'). In this study, the predictors are the diesel/biodiesel fuel-blend heating value and prepared volume fraction. This modeling is realized by extracting from the predictors a set of orthogonal factors called 'latent variables', which have the best predictive power [39]. A full description of the PLS regression is given by Wold et al. [40].

Support vector machines (SVMs) [41, 42] is a method that is based on statistical learning theory, trained through a supervised learning algorithm that can be applied to problems of classification or regression. In general, SVM is recommended for situations in which

the dataset has non-linear behavior [43, 44]. There are many kernel functions that can be used to work with SVM. These functions project the original dataset into a three-dimensional feature space by adding an additional dimension and separating the linearly inseparable data. A full description of the SVM method is given by Ivanciuc [45].

This study examined the performance of PLS and SVM, as applied to the LDTR thermograms, to quantify a range of diesel/biodiesel fuel blends and corresponding heating values. This required measurement repeatability that enabled the chemometric approaches to provide successful correlation of the predicted values with the measurements.

2. Fuel samples and experimental methods

2.1 Fuel samples and preparation of the diesel/biodiesel fuel blends

The National Institute of Standards and Technology (NIST) provides a variety of fuel-related Standard Reference Material[®]s (SRM[®]s). While typically certified for chemical composition rather than thermochemical properties, these SRMs are known sources of well-characterized, homogeneous, and stable materials. Two SRMs were used in this investigation, namely, SRM 2770 'Sulfur in Diesel Fuel Oil' (a commercial 'No. 2-D' distillate fuel oil) [46] and SRM 2772 'B100 Biodiesel' (a commercial 100 % biodiesel produced from soy) [47]. These referenced certificates of analysis provide the available information for the chemical analysis and physical properties of each fuel. Note that the fuel composition was assumed to be unchanged during these experiments; NIST issues new certificates of analysis when constituents are found to change significantly. Nine binary mixtures were prepared from these two SRMs, varying in volume fraction (v/v) from 90 % diesel/10 % biodiesel to 10 % diesel/ 90 % biodiesel. A milliliter of liquid was prepared for each mixture sample using a syringe (0.5 mL maximum). It is noted that due to preferential vaporization of the many diesel and biodiesel fuel components, the blend temperature-dependent, instantaneous volume fraction can vary during heating of the sample; these effects are captured features within the thermograms [37,38].

2.2 Experimental arrangement

The experimental arrangement is illustrated in Figs. 1 and 2. A drop of liquid sample was placed (using a syringe) onto a copper pan (inner diameter: (4.95 ± 0.01^1) mm, height: (2.34 ± 0.01) mm, thickness: (0.125 ± 0.001) mm, mass: (50.2 ± 0.2) mg) located in the middle of a sphere-shaped copper reactor (diameter: (18.2 ± 0.1) mm, and thickness: ≈ 0.03 mm, mass: (2.22 ± 0.07) g). The reactor was centrally stationed within a stainless-steel chamber with several glass-enclosed ports. The reactor sphere was fabricated in-

¹ Estimation of the measurement uncertainty for this study is determined from analysis of a series of replicated measurements (referred to as Type A evaluation of uncertainty), and from means other than statistical analysis (referred to as Type B evaluation of uncertainty) [48]. The Type A uncertainty is calculated as $k_c u_c$, where k_c is the coverage factor and u_c is the combined standard uncertainty. The value for u_c is estimated as $sn^{-1/2}$, where s is the sample standard deviation and n is the number of independent measurements. For $n = 2, 3,$ and 50 , $k = 4.30, 3.18,$ and 2.01 , respectively, representing a level of confidence of 95 %.

house, by reworking two thin copper sheets into two hemispheres using a stainless-steel ball and hollowed-out copper form [36]. Excess copper from each newly formed hemisphere was cut away leaving a small tab with a tapped hole on each side. The two hemispheres were attached together with supporting wires passing through each hole. Each wire then passed through ceramic tubes that insulated the wires and affixed the sphere to a copper frame surrounding the sphere, as shown in Fig. 2. A customized Omega² K-type, fine-wire thermocouple (0.25 mm bead diameter, unsheathed, 0.200 s ± 0.002 s response time, see insert in Fig. 1) was bent into a cardioid shape to provide surface area for supporting the copper pan near the center of the reactor. Three thermocouple wires were stretched across the pan bottom by attaching the ends of the wires to the pan wall. Slipping the bent thermocouple wire between the three suspension wires and the bottom of the pan ensured that the outer surface of the pan bottom sat stably on, and remained in thermal contact with, the thermocouple bead. A second thermocouple (same type) was bent and in contact with the reactor inner surface at a location near the center of the hemisphere and laser beam impingement site.

The assembly procedure for the reactor sphere was first to slip the pan onto the cardioid-shaped thermocouple (set in the middle of the fabricated support frame), see Fig. 1. The tab of one hemisphere was inserted through the post from one arm of the frame. The post was bent with a right angle (horizontally) to support the hemisphere while maneuvering the other end of the hemisphere to the frame second side and slipping the other pin through the sphere tab. After checking that the pan was centered within the hemisphere, the second hemisphere was slipped over the two outward facing pins. The pins were then bent against the sphere edge with pliers to secure the sphere.

The reactor assembly was heated from opposing sides by a 250 W, continuous-wave, near-infrared Nd:YAG laser beam (operating at a wavelength of 1.064 μm) with nearly uniform sample temperature near the center of the sphere [35]. The reactor sphere acts as a thermal lens to focus the radiative heat transfer to a small region at its center where the sample and pan are stationed. The temperature at the center of the sphere was checked in the past to be uniform [35]. The sphere dimensions, wall thickness, and thermal conductivity were chosen to maximize the radiative (and minimize convective) heat transfer.

Laser heating of the reactor sphere has several advantages over direct electrical-resistance heating of the pan (see Ref. [36]). First, use of an appropriate heating rate and sample mass ensures detection of fuel chemical reactions in the thermogram features. Too small a sample mass can lead to issues regarding its equivalency to the bulk-material thermal characteristics. Heating rates too slow or fast may lead to biased results - preferential vaporization of chemical constituents can influence results obtained with slower heating rates; capturing chemical reactions with ultrahigh heating rates can also be an issue. Second, laser heating enables direct radiative heat transfer

² Certain commercial equipment or materials are identified in this publication to specify adequately the experimental procedure. Such identification does not imply recommendation or endorsement by the National Institute of Standards and Technology, nor does it imply that the materials or equipment are necessarily the best available for this purpose.

to the sample from the reactor, being the dominant mode of heat transfer at high temperature. Radiation does not disturb the surrounding air as does convection. With electrical heating, the main mode of heat transfer is conduction through the pan and then convection to the sample, leading to nonuniform heat transfer to the sample. Note that the reaction sphere dimensions were designed to minimize the pan distance to the reactor walls in order to reduce convective heat transfer (corresponding to a small Nusselt number) to the surrounding gas. The reactor was supported on a post to enable easy removal of the assembly from within the chamber, which was used to ensure control of the environment around the sample. Measurements were carried out at laboratory ambient pressure. The thermocouple temperature readings of the sample/pan and reactor surface were recorded with respect to time at a sampling rate of 100 Hz by the data acquisition system. The temperatures were reported every 0.25 s because of the limited thermocouple response time.

Experiments were carried out without sample (providing a 'baseline' thermogram for both the sample and reactor thermocouples) and with sample ('sample' thermogram and 'reactor' thermogram). For each fuel, four thermograms were obtained having a calculated standard uncertainty for all temperatures throughout the four thermograms of better than 2.5 K (Type A uncertainty; the Type B uncertainty was estimated by the manufacturer to be 1.1 K). This required that the initial time and temperature for each run be approximately the same.

2.3 Measurement protocol

Preparation for an experimental run entailed preheating a new sphere and pan above 773 K to form a black copper oxide layer on all exposed surfaces [37]. With a syringe, one 5 μL liquid droplet (mass of (4.0 ± 0.1) mg for SRM 2770 and (4.4 ± 0.1) mg for SRM 2772) was injected into the copper pan. The chamber lid was then closed to isolate the liquid from the surrounding environment (with the chamber pressure remaining at that of the laboratory). The syringe was set to provide an approximate 5 μL droplet, because it was determined beforehand to provide enough mass to express the sample exothermic behavior (i.e., formation of peaks above the baseline in the thermogram temperature-time derivative profile). Injecting a droplet on the pan through the opening in the top of the sphere ensured that the pan position remained unchanged inside the reactor sphere. This procedure reduced the uncertainty of realignment of the pan and laser beams for each run.

An experimental run was initiated by starting the data acquisition program and pressing after about 5 s a remote switch to open the laser shutter. The laser power output was set to provide 134 W and remained unchanged for all experiments. The laser power was not connected directly to the data acquisition program, so the start time of each run (when the laser shutter was opened, causing the temperature to rise) did not always occur at the same time step. With the laser shutter open, the sample was heated until the system reached near-steady-state temperature (i.e., complete consumption of the sample). At this point, the laser shutter was closed, which allowed the temperature to return to the laboratory ambient and terminate the run. While cooling (at about 573 K), the reactor sphere was momentarily reheated back to 773 K to re-establish the copper

oxide layer on the pan and sphere inner/outer surfaces. An initial baseline run (i.e., without sample) was completed before carrying out measurements with fuel. Four fuel runs were carried out to confirm measurement repeatability. Afterwards, several additional baselines were obtained to monitor changes in the sphere condition.

During a run, the two thermocouple temperatures were recorded by the data acquisition software. The resulting thermograms from each experiment were used to evaluate the sample thermal exothermic behavior. See Ref. [36] for a discussion regarding the possible formation and effect of a fuel vapor layer above the pan surface on the reported sample temperature. Expressions for the specific energy release rate and total specific energy release (i.e., gross heating value; enthalpy of combustion) were derived from an equation for thermal energy conservation [35]. A computer-based spread sheet was developed to enable data processing and evaluation.

2.4 Sphere/Pan lifetime

The lifetime of a single reactor sphere (thickness of ≈ 0.02 mm) was about ten experimental runs before replacement (i.e., essentially one sphere to evaluate each fuel blend). The sphere lifetime was limited by the repeated heating and re-oxidation of the sphere, which caused the surface to degrade in time. The oxidized copper surface visually appears to become brittle (see Fig. 3A), ultimately resulting in penetration of the laser beam through the sphere surface - thus requiring replacement. Note that the copper pan was also oxidized and subject to the same thermal degradation, but over a much longer period. The sphere diameter also expanded (as well as increased in mass due to buildup of the oxide layer) with repeated heating (see Fig. 3B), which resulted in a decrease of the maximum achievable steady-state temperature after several runs. The sphere was replaced when the maximum temperature was reduced by about 20 %, or when the sphere was observed to be significantly distorted and its diameter expanded, as shown in Fig. 3. Sometimes the sphere was removed and reshaped with the stainless-steel ball to extend its life. This was done so long as the sphere diameter was not too large. The installation procedure outlined above was repeated when replacing the sphere or pan. Several experimental design changes (e.g., using thicker copper stock, making smaller diameter spheres requiring less laser power to achieve similar heating rates and temperatures as with the current arrangement) are currently underway to extend the sphere lifetime, however such changes will affect the heat transfer processes, and require detailed evaluation.

2.5 Thermogram repeatability

In addition to the reduced steady-state temperature with each successive run due to sphere degradation, care was also required to start each run at the same initial time and temperature to minimize the differences between thermograms. For prior experiments, not considering these three factors, the repeatability had a computed standard uncertainty of 2.5 K, at best, for four replicate thermograms. The standard uncertainty was computed by determining the arithmetic mean and variance of the thermogram temperatures at each time step. The variance for all the time steps was pooled and used to obtain an overall standard uncertainty. Experimentally, the above-mentioned

uncertainty would be considered relatively small, however, better thermogram repeatability was required for the chemometric computations. This was achieved by starting each run at nearly the same initial (laboratory) temperature and using the data post-processing procedures discussed next to 1) optimize alignment of each run start time and 2) match the thermogram steady-state temperatures. The computed standard uncertainty was reduced to better than 2.0 K for four replicate thermograms and enabled successful application of the chemometrics.

2.6 Data post-processing

As noted above, differences in run start times and the decrease in steady-state temperature with repeated heating of the sphere resulted in temperature differences between thermograms. These temperature differences were associated with the initial and final steady-state portions of the thermograms. They did not mask experimental uncertainties associated with measurement of the sample thermochemical response to laser heating (i.e., exothermic portion of the thermogram, which is affected by the initial sample mass, position of the pan on the thermocouple, alignment of the laser beams, variability in the input laser power, etc.). Since these two issues could not be handled experimentally at this time, an alternative approach was developed to address them computationally. Better matching of these nonreacting segments of the thermograms enabled the chemometric computations to be carried out successfully.

To minimize the differences between sample start times and steady-state temperatures, as well as when compared with a baseline, a spread sheet was developed to translate the thermograms to best match their run start times and extrapolate to best match their steady-state temperatures. This automated thermogram translation/extrapolation protocol ensured that the initial and final run temperatures matched while not affecting the portion of the thermogram displaying the sample thermochemistry. The best matching among the four curves was determined by minimizing the pooled standard uncertainty of all the measurement points for the entire thermogram.

To translate and match one curve with a second stationary curve (defined for the thermogram with the highest steady-state temperature at the end of the run), the objective was not just to match the initial start time but to minimize the uncertainty over the entire curve. Since the matching was between repeated runs, ideally there should be no difference between the runs. Thus, the translated-curve temperatures should be identically associated with the stationary-curve temperatures and run times. In fact, when shifted all temperatures for the translated curve do not overlap those of the stationary curve. Thermograms can be aligned and compared after completion of a run, but only by the set time interval of the data acquisition system. This may not result in the optimal matching of the curves, so it becomes necessary to translate the curves by fractional sampling intervals. Shifting the translation curve in this manner optimizes the matching between curves, but the translated temperatures (being an array of points) will be associated with different run times than that of the stationary curve (being the data acquisition times). One must therefore interpolate temperatures from the translated curve to align with the stationary-curve times, so that the temperatures

for both curves are associated with the same array of run times. The translated-curve temperatures were thus modified according to:

$$T_{m,i}(t_{s,i}) = T_{m,j} + \left[\frac{T_{m,j} - T_{m,j-1}}{t_{m,j} - t_{m,j-1}} \right] [t_{s,i} - t_{m,j}] \quad (1)$$

for $t_{m,j-1} < t_{s,i} < t_{m,j}$. Here, T is the temperature, t is the time, i and j are the indices for each sample array, and subscripts m and s refer to the translated and stationary thermograms, respectively.

The procedure for extrapolating thermogram final steady-state temperatures follows a procedure described in an earlier article [36], which matched four sample runs with the baseline to enable quantitative evaluation of the sample thermochemical characteristics. The procedure used in this investigation compared three thermograms to be extrapolated with the fourth stationary thermogram (i.e., having the highest steady-state temperature). Since multiple inflection points may be present as a result of the sample thermal decomposition, the extrapolation was started at the inflection point where the temperature relaxed back to the baseline temperature. The extrapolated thermograms were shifted (stretched) to the higher stationary-curve temperatures with the extrapolated-curve derivatives kept unchanged (i.e., peak values of the derivative profile, which correspond to the thermogram inflection points). This procedure preserved the curvature of each thermogram and matched the steady-state temperature of all four thermograms.

The procedure entails first updating the time of each extrapolated thermogram (with subscript m), while maintaining the same maximum slope of the extrapolated curve and using the unchanged stationary thermogram temperatures, according to:

$$t_{m,j} = t_{s,i} + \frac{(T_s - T_m)_i}{\left(\frac{dT}{dt}\right)_{m,max}} \quad (2)$$

and defining the extrapolated-curve derivatives by:

$$\left(\frac{dT}{dt}\right)_{m,j} = \frac{T_{s,i} - T_{s,i-1}}{t_{m,j} - t_{m,j-1}} \quad (3)$$

for $t_i > t_i[(dT/dt)_{m,max}]$. After the updated values of time $t_{m,j}$ and the derivative $(dT/dt)_{m,j}$ are known, the new extrapolated temperatures, $T_{m,i}$ (corresponding to the fixed stationary-curve times from the data acquisition system) are determined by:

$$T_{m,i} = T_{s,j-1} + (t_{s,i} - t_{m,j-1}) \left(\frac{dT}{dt}\right)_{m,j} \quad (4)$$

where $t_{m,j} < t_{s,i} < t_{m,j+1}$.

The raw data for each fuel blend was manipulated in two stages: 1) translation/extrapolation of the four thermograms for a specific fuel blend, and 2) translation/extrapolation to the highest steady-state temperature among all fuel blends. An example for SRM 2772 is provided in Fig. 4, which presents the raw experimental thermogram and derivatives (with respect to sample temperature) in Fig. 4A, the translated thermograms in Fig. 4B, and the extrapolated thermograms in Fig. 4C (i.e., three translated runs matched to the fourth stationary thermogram with the highest steady-state temperature). The standard uncertainty reported for the four replicates decreased by about 59 % from the original measured thermograms to the final translated/extrapolated curves.

Also presented in Fig. 4 is the corresponding variation in the temperature-time derivative with sample temperature. The two peaks observed in the temperature-time derivatives of Figs. 4 are attributed to preferential vaporization and reaction of the fuel constituents: the lower-temperature peak corresponding to vaporization of the lighter fractions, while the heavier fractions continue to vaporize and then react at higher temperature (second peak), see Refs. [37,38]. The constituents of the pure biodiesel fuel SRM 2772 are fatty acid methyl esters with boiling points somewhat higher than that of the hydrocarbon diesel fuel SRM 2770, which results in the lower-temperature peak trending to higher temperatures. These derivative profiles in Fig. 4 remain unchanged except for the improved matching at the steady-state temperature, indicating that the fuels react similarly for each run and that the measurement is repeatable. Figure 4 demonstrates the improved matching between thermograms (while not affecting the reactive portion of the profiles), which was necessary for the successful application of these experimental data to the chemometric models.

2.7 Determination of the total specific energy release

The details of the model used to estimate the thermochemical characteristics (i.e., specific energy release rate and total specific energy release) are described elsewhere (e.g., Refs. [36, 37]). The calculations are based on an equation for the conservation of thermal energy, given by:

$$m(t)c_p(T) \frac{dT}{dt} = IA\beta(T, \lambda) - F(T, T_o) + \Delta m(t)q(T) \quad (5)$$

where the term on the left side is the internal energy of the sample (for mass m and specific heat capacity c_p). The first term on the right side is the energy input by the laser (of beam intensity I , cross-sectional area A , absorptivity β , and wavelength λ), followed by the total energy release F (at a reference temperature T_o) due to heat transfer processes (conduction, convection, and radiation). The last term is the energy gain/loss due to chemical decomposition, phase change, and reactions (for changing sample mass Δm and a specific energy release rate q). Analysis of all terms in the above-mentioned energy balance equation enables estimation of $q(T)$. Integration (using the trapezoidal rule) of the positive exothermic values for $q(T)$ leads to estimation of the total specific energy release, i.e., $Q = \int q(T)dT$. Estimation of Q was carried out by analyzing the heat transfer processes to the surrounding environment for the heated sample contained

within the sphere volume ('sphere' analysis) [36]. The calculated heating values for the unblended SRMs were comparable to those in the literature [37]. Figure 5 presents the calculated values for Q with respect to prepared fuel-blend volume fraction (averaging all four sample replicates for each blend). The error bars represent the expanded uncertainty (95 % confidence level).

3. Chemometric results and discussion

All calculations were performed using PLS toolbox version 3.5.1 (Eigenvector Research, Manson, WA) running in MATLAB R2014b.

3.1 Quantification of fuel-blend characteristics by multivariate calibration methods

Multivariate calibration methods were used to train algorithms to quantify the 1) prepared fuel-blend volume fraction and 2) total specific energy release (heating value) of the diesel/biodiesel fuel blends, i.e., for one diesel fuel, one biodiesel fuel, and nine diesel/biodiesel blends (each fuel with four replicates), thus a total of 44 thermograms. These methods were compared for accuracy using three types of error analyses, namely, the root mean square error of calibration (RMSEC), root mean square error of cross validation (RMSECV), and root mean square error of validation (RMSEP). The calibration methods chosen were the linear partial least squares (PLS) model and nonlinear support vector machine (SVM) model. The PLS model attempts to fit data linearly by inferring a relationship between the fuel thermochemical characteristics and thermograms. Performance is best if the relationship between the fuel characteristics and thermograms is known so that it can be used to interpolate and predict other cases. It can work well even with a limited training set [43]. The SVM model is a nonlinear modeling technique that has been applied to chemometrics problems since it can fit the data linearly or nonlinearly [49, 50]. While good performance by either the SVM model or PLS model would be an indicator of the utility of using multivariate calibration methods to quantify thermal calorimetry data, the SVM model will likely outperform PLS, unless the training data has a linear mathematical relationship [51].

3.2 Model evaluation

Several preprocessing techniques were tested, including autoscaling, mean-centering, generalized-least-squares-weighting, and their combinations. The three error analyses RMSEC, RMSECV, and RMSEP were used to compare each preprocessing technique. The results indicated that the best estimation for both prepared fuel-blend volume fraction and heating value was the mean-centering technique.

The number of thermograms used to build and validate each chemometric model was 30 and 14 (total of 44 thermograms), respectively, resulting in the formation of the following matrices: $X_{calibrations}$ (30 x 101) and $X_{validation}$ (14 x 101), as well as vectors $Y_{calibration}$ (30 x 1) and $Y_{validation}$ (14 x 1). The Kennard-Stone algorithm [52] was used to populate these matrices. Figure 6 presents the correlation of the predicted values with the measured values for the range of prepared fuel-blend volume fractions, using the PLS (Fig. 6A) and SVM (Figs. 6C) algorithms with mean-centering preprocessing. The

corresponding residuals (i.e., percent difference between the estimated calibrated data points and the calibration line) are provided in Figs. 6B and 6D, respectively. Similarly, Fig. 7 presents the predictions for the fuel-blend total specific energy release. The figures indicate reasonable correlation between the model predictions and measured values for the nonlinear SVM model (Figs. 6C and 7C), while the linear PLS model (Figs. 6A and 7A) does not correlate as well. The error is greater for the total specific energy release than for the fuel-blend volume fraction because of the uncertainty associated with calculating this quantity. In addition, the corresponding residuals for the SVM model (Figs. 6D and 7D) are smaller than the PLS results (Figs. 6B and 7B), which also indicates better correlation.

Table 1 presents a comparison of the different error-analysis results, as applied to both the PLS and SVM calibration models. The table lists results for the following error analyses: RMSCE, RMSECV, RMSEP, as well as the Pearson's correlation coefficient between the measured and predicted properties during the validation (R_{val}), and Pearson's correlation coefficient between the real and predicted properties for the calibration (R_{cal}). For the PLS model, the number of latent variables (LVs) was chosen by leave-one-out cross validation [53-55], in which all calibration samples were validated one by one. The number of LVs chosen was based on the lowest obtained RMSECV value. A satisfactory prediction performance was based on obtaining values of the Pearson's correlation coefficient close to 1. As indicated in Table 1, the RMSEC and RMSEP values for the SVM model were lower than those for the PLS model. The values of the Pearson's correlation coefficient for the SVM model was higher than for the PLS model, and close to 1.

A F-test [56] for a 95 % confidence level (i.e., for the fraction of the distribution $p = 0.05$) was also performed, considering the null hypothesis that there was no significant difference between the PLS and SVM models for the fuel-blend total specific energy release and fuel-blend volume fraction. For the F -test [56], the following expression was used:

$$F = \frac{(RMSEP_i)^2}{(RMSEP_j)^2} \quad (6)$$

where RMSEP is the root mean square error of prediction (that is, the model prediction of the validation set) and the subscripts i and j represent the models with the larger and smallest RMSEP values, respectively. The degrees of freedom in the F -test was 29 for both models. The F value corresponding to a confidence level of 95 % was 1.86. The F -test results were 1.6 and 3.30 for the total specific energy release and prepared volume fraction, respectively. Thus, the PLS and SVM models are considered equivalent for the total specific energy release but nonequivalent for the prepared volume fraction; i.e., either the SVM or PLS model can be used to quantify the total specific energy release, while the SVM algorithm better represents the prepared volume fraction results.

3.3 Challenges in modeling the experimental results

The PLS and SVM models were also used to predict the boiling-point temperature for the diesel/biodiesel fuel mixtures. It was thought that the lower-temperature peak in the thermogram derivative profiles (see Fig. 8) would be representative of the fuel boiling-point temperature because the peak temperatures for the pure fuels were similar to the values in the literature: 444 K - 633 K [46] for SRM 2770 diesel fuel and < 583 K [37] for SRM 2772 biodiesel fuel. The dashed curve in Fig. 8 illustrates the estimated trend in boiling point for all the fuel mixtures.

Both chemometric models were unable to predict the boiling-point temperature trend. Again, the SVM model prediction was better than the PLS model, but the error analysis results indicated relatively poor correlation (RMSEC = 3.33 K, RMSEP = 26.36 K, Rcal = 0.99, and Rval = 0.59). As seen in Fig. 8, the lower-temperature peak in the derivative profile for each fuel mixture is relatively broad since the boiling-point temperature is really a range of values, not a single value. This fact is not simulated by either chemometric model, which are both static (single-point) algorithms. Consequently, it would be expected for the model output to have a substantial error when trying to reproduce a boiling-point range with only a single representative value. Efforts were also made to average the boiling-point range differently, but the result was the same. Determining how to model the boiling point of complex mixtures such as fuels for use in chemometrics could be the subject of future research.

4. Conclusions

In this work, linear and nonlinear multivariate calibration methods were used to estimate physical and chemical properties of fuels using laser-driven calorimetry thermograms. The successful application of multivariate calibration methods was based on providing highly repeatable calorimetry thermograms, which required careful understanding and remediation of issues affecting the calorimetry measurements. The properties investigated included total specific energy release (heating value) and prepared volume fraction of eleven different diesel/biodiesel fuel blends.

The results demonstrated that it is possible to predict the total specific energy release and prepared volume fraction of diesel/biodiesel fuel blends when employing either the PLS or SVM model for chemometric analysis of laser-driven calorimetry thermograms. The PLS and SVM models showed similar results for estimating the heating value. The SVM model was best suited for reproducing the prepared fuel-blend volume fraction. The next step is to extend this investigation to quantification of other thermophysical and thermochemical fuel-blend characteristics.

Acknowledgements

The authors thank Dr. P. Chu for her helpful suggestions.

Nomenclature

A	cross-sectional area [m ²]
$c_p(T)$	specific heat capacity [J g ⁻¹ K ⁻¹]
$F(T, T_o)$	total energy loss due to heat transfer [W]
I	intensity [W m ⁻²]
k	subgroup
k_c	coverage factor
$m(t)$	mass [g]
n, N	sample size
p	fraction of the distribution
$q(T)$	specific energy release rate [kW g ⁻¹]
Q	total specific energy release [kJ g ⁻¹]
R	correlation coefficient
R^2	determination coefficient
s	standard deviation
t	time [s]
T	temperature [K]
u_c	combined standard uncertainty
v/v	prepared volume fraction [%/%]
W	Levene's test
X	matrix of independent variables
Y	matrix of dependent variables
Z_{ij}	mean of the subgroup
$\bar{Z}_{i.}$	mean of the group
$\bar{Z}_{i..}$	overall mean of all groups

Greek symbols

β	absorptivity
$\Delta m(t)$	change in mass [g]
λ	wavelength [m]

Subscripts

i, j	index
m	translation
s	stationary
o	reference

References

1. Miles, P., *Efficiency merit function for spark ignition engines: Revisions and improvements based on FY16–17 research*; Report No. DOE/GO-102018-5041, U.S. Department of Energy. 2018; Available from: https://www.energy.gov/sites/prod/files/2018/02/f48/Co-Optima%20Merit%20Function%20Report%2067584_2.pdf.
2. Alves, J.C.L.; Henriques, C.B.; Poppi, R.J. Determination of diesel quality parameters using support vector regression and near infrared spectroscopy for an in-line blending optimizer system. *Fuel*, **2012**. *97*, 710-717.
3. Kelly, W.R.; MacDonald, B.S.; Leigh, S.D., *A method for the preparation of NIST traceable fossil fuel standards with concentrations intermediate to SRM values*; Report No. National Institute of Standards and Technology, Gaithersburg, MD. NIST Special Publication (SP) 1074. 2007.
4. Balabin, R.M.; Safieva, R.Z. Biodiesel classification by base stock type (vegetable oil) using near infrared spectroscopy data. *Anal Chim Acta*, **2011**. *689*, 190-197.
5. Barros, T.F.S.; Arriel, N.H.C.; Queiroz, M.F.; Fernandes, P.D.; Mendonca, S.; Ribeiro, J.A.A.; Medeiros, E.P. Fatty acid profiles of species of *Jatropha curcas* L., *Jatropha mollissima* (Pohl) Baill. and *Jatropha gossypifolia* L. *Ind Crop Prod*, **2015**. *73*, 106-108.
6. Brandao, L.F.P.; Braga, J.W.B.; Suarez, P.A.Z. Determination of vegetable oils and fats adulterants in diesel oil by high performance liquid chromatography and multivariate methods. *J Chromatogr A*, **2012**. *1225*, 150-157.
7. Brown, C.; Dean, R.; Hupp, A. Investigation of biodiesel-diesel blends using GCMS and PCA. *Abstr Pap Am Chem S*, **2017**. *253*.
8. Constantino, A.F.; Lacerda, V.; dos Santos, R.B.; Greco, S.J.; Silva, R.C.; Neto, A.C.; Barbosa, L.L.; de Castro, E.V.R.; Freitas, J.C.C. Analysis of Oil Content and Oil Quality in Oilseeds by Low-Field NMR. *Quim Nova*, **2014**. *37*, 10-17.
9. Dean, R.; Brown, C.; Hupp, A. Investigation of biodiesel-diesel blends using GCMS and PCA. *Abstr Pap Am Chem S*, **2016**. *251*.
10. dos Santos, V.H.J.M.; Bruzza, E.D.; de Lima, J.E.; Lourega, R.V.; Rodrigues, L.F. Discriminant analysis and cluster analysis of biodiesel fuel blends based on fourier transform infrared spectroscopy (FTIR). *Energ Fuel*, **2016**. *30*, 4905-4915.
11. Fan, Z.; Schroder, O.; Krahl, J. Analysis of diesel fuels/biodiesel blends and identification of biodiesel using time-resolved laser-induced fluorescence spectroscopy (TRLFS). *Landbauforschung-Ger*, **2015**. *65*, 1-14.
12. Felizardo, P.; Baptista, P.; Uva, M.S.; Menezes, J.C.; Correia, M.J.N. Monitoring biodiesel fuel quality by near infrared spectroscopy. *J Near Infrared Spec*, **2007**. *15*, 97-105.
13. Flood, M.E.; Goding, J.C.; O'Connor, J.B.; Ragon, D.Y.; Hupp, A.M. Analysis of biodiesel feedstock using GCMS and unsupervised chemometric methods. *J Am Oil Chem Soc*, **2014**. *91*, 1443-1452.
14. Alves, J.C.L.; Poppi, R.J. Biodiesel content determination in diesel fuel blends using near infrared (NIR) spectroscopy and support vector machines (SVM). *Talanta*, **2013**. *104*, 155-161.
15. de Oliveira, I.K.; Rocha, W.F.D.; Poppi, R.J. Application of near infrared spectroscopy and multivariate control charts for monitoring biodiesel blends. *Anal Chim Acta*, **2009**. *642*, 217-221.
16. Cui, C.; Zhang, L.Z.; Ma, Y.J.; Billa, T.; Hou, Z.; Shi, Q.; Zhao, S.Q.; Xu, C.M.; Klein, M.T. Computer-aided gasoline compositional model development based on GC-FID analysis. *Energ Fuel*, **2018**. *32*, 8366-8373.

17. Zanao, L.R.; dos Santos, B.C.D.B.; Sequinel, R.; Flumignan, D.L.; de Oliveira, J.E. Prediction of relative density, distillation temperatures, flash point, and cetane number of S500 diesel oil using multivariate calibration of gas chromatographic profiles. *Energ Fuel*, **2018**. *32*, 8108-8114.
18. Mabood, F.; Boque, R.; Hamaed, A.; Jabeen, F.; Al-Harrasi, A.; Hussain, J.; Alameri, S.; Albroumi, M.; Al Nabhani, M.M.O.; Naureen, Z.; Al Rawahi, M.; Al Futaisi, F.A.S. Near-Infrared spectroscopy coupled with multivariate methods for the characterization of ethanol adulteration in premium 91 gasoline. *Energ Fuel*, **2017**. *31*, 7591-7597.
19. Ouyang, A.G.; Zhang, Y.; Cheng, M.J.; Wang, H.Y.; Liu, Y.D. Determination of the content of ethanol in ethanol gasoline using mid-infrared spectroscopy. *Chin Opt*, **2017**. *10*, 752-760.
20. Balabin, R.M.; Safieva, R.Z.; Lomakina, E.I. Gasoline classification using near infrared (NIR) spectroscopy data: Comparison of multivariate techniques. *Anal Chim Acta*, **2010**. *671*, 27-35.
21. da Silva, N.C.; Pimentel, M.F.; Honorato, R.S.; Talhavini, M.; Maldaner, A.O.; Honorato, F.A. Classification of Brazilian and foreign gasolines adulterated with alcohol using infrared spectroscopy. *Forensic Sci Int*, **2015**. *253*, 33-42.
22. Ferreiro-Gonzalez, M.; Ayuso, J.; Alvarez, J.A.; Palma, M.; Barroso, C.G. Gasoline analysis by headspace mass spectrometry and near infrared spectroscopy. *Fuel*, **2015**. *153*, 402-407.
23. Matuszewska, A.; Odziemkowska, M.; Czarnocka, J. Use of infrared spectroscopy to study changes in gasolines during storage. *Przem Chem*, **2015**. *94*, 1300-1304.
24. de Carvalho Rocha, W.F.; Nogueira, R.; Vaz, B.G. Validation of model of multivariate calibration: An application to the determination of biodiesel blend levels in diesel by near-infrared spectroscopy. *Journal of Chemometrics*, **2012**. *26*, 456-461.
25. Filgueiras, P.R.; Sad, C.M.S.; Loureiro, A.R.; Santos, M.F.P.; Castro, E.V.R.; Dias, J.C.M.; Poppi, R.J. Determination of API gravity, kinematic viscosity and water content in petroleum by ATR-FTIR spectroscopy and multivariate calibration. *Fuel*, **2014**. *116*, 123-130.
26. Obeidat, S.M. The use of H-1 NMR and PCA for quality assessment of gasoline of different octane number. *Appl Magn Reson*, **2015**. *46*, 875-883.
27. Burger, J.L.; Widegren, J.A.; Lovestead, T.M.; Bruno, T.J. H-1 and C-13 NMR Analysis of gas turbine fuels as applied to the advanced distillation curve method. *Energ Fuel*, **2015**. *29*, 4874-4885.
28. Elbaz, A.M.; Gani, A.; Hourani, N.; Emwas, A.H.; Sarathy, S.M.; Roberts, W.L. TG/DTG, FT-ICR mass spectrometry, and NMR spectroscopy study of heavy fuel oil. *Energ Fuel*, **2015**. *29*, 7825-7835.
29. Bouhadda, Y.; Fergoug, T.; Sheu, E.Y.; Bendedouch, D.; Krallafa, A.; Bormann, D.; Boubguira, A. Second order Raman spectra of Algerian Hassi-Messaoud asphaltene. *Fuel*, **2008**. *87*, 3481-3482.
30. Lapuerta, M.; Oliva, F.; Agudelo, J.R.; Stitt, J.P. Optimization of Raman spectroscopy parameters for characterizing soot from different diesel fuels. *Combust Sci Technol*, **2011**. *183*, 1203-1220.
31. Abdallah, W.A.; Yang, Y. Raman spectrum of asphaltene. *Energ Fuel*, **2012**. *26*, 6888-6896.
32. Cordeiro Dantas, W.F.; Laurentino Alves, J.C.; Poppi, R.J. MCR-ALS with correlation constraint and Raman spectroscopy for identification and quantification of biofuels and adulterants in petroleum diesel. *Chemometr Intell Lab*, **2017**. *169*, 116-121.
33. Gobel, A.; Hemberger, F.; Vidi, S.; Ebert, H.P. A new method for the determination of the specific heat capacity using laser-flash calorimetry down to 77 K. *Int J Thermophys*, **2013**. *34*, 883-893.

34. Roth, E.P., *Measurement of thermal conductivity from high temperature pulse diffusivity and calorimetry measurements*, in *Thermal Conductivity 18*, T. Ashworth and D.R. Smith, eds. 1985, Springer: Boston, MA.
35. Nazarian, A.; Presser, C. Thermal and chemical kinetic characterization of multiphase and multicomponent substances by laser heating. *Int J Heat Mass Tran*, **2008**. *51*, 1365-1378.
36. Presser, C.; Nazarian, A. Laser-driven calorimetry of single-component liquid hydrocarbons. *Energ Fuel*, **2017**. *31*, 6732-6747.
37. Presser, C.; Nazarian, A.; Bruno, T.J.; Murray, J.A.; Molloy, J.L. Thermochemical characterization of bio- and petro-diesel fuels using a novel laser-heating technique. *Energ Fuel*, **2015**. *29*, 5761-5772.
38. Presser, C.; Nazarian, A.; Millo, A. Laser-driven calorimetry measurements of petroleum and biodiesel fuels. *Fuel*, **2018**. *214*, 656-666.
39. Abdi, H. Partial least squares regression and projection on latent structure regression (PLS regression). *Computational Statistics*, **2010**. doi:10.1002/wics.051.
40. Wold, S.; Sjostrom, M.; Eriksson, L. PLS-regression: A basic tool of chemometrics. *Chemometr Intell Lab*, **2001**. *58*, 109-130.
41. Cristianini, N.; Shawe-Taylor, J., *An introduction to support vector machines and other kernel-based learning methods*. doi:DOI: 10.1017/CBO97805118013892000, Cambridge: Cambridge University Press.
42. Vapnik, V.N., *The nature of statistical learning theory*. 1995: Springer-Verlag. 188.
43. Vaz, B.G.; Abdelnur, P.V.; Rocha, W.F.C.; Gomes, A.O.; Pereira, R.C.L. Predictive petroleomics: measurement of the total acid number by electrospray fourier transform mass spectrometry and chemometric analysis. *Energ Fuel*, **2013**. *27*, 1873-1880.
44. Luna, A.S.; Lima, I.C.A.; Rocha, W.F.C.; Araujo, J.R.; Kuznetsov, A.; Ferreira, E.H.M.; Boque, R.; Ferre, J. Classification of soil samples based on Raman spectroscopy and X-ray fluorescence spectrometry combined with chemometric methods and variable selection. *Anal Methods-Uk*, **2014**. *6*, 8930-8939.
45. Ivanciuc, O., *Applications of support vector machines in chemistry*, in *Reviews in Computational Chemistry*. 2007. p. 291-400.
46. *SRM 2770; Sulfur in diesel fuel oil (nominal mass fraction 40 mg/kg)*; National Institute of Standards and Technology; U.S. Department of Commerce. Gaithersburg, MD, USA, 02 May 2016.
47. *SRM 2772; B100 biodiesel (soy-based)*; National Institute of Standards and Technology; U.S. Department of Commerce. Gaithersburg, MD, USA, 20 October 2016.
48. Taylor, B.N.; Kuyatt, C.E., *Guidelines for evaluating and expressing the uncertainty of NIST measurement results*; Report No. Gaithersburg, MD, 1994.
49. Filgueiras, P.R.; Alves, J.C.L.; Poppi, R.J. Quantification of animal fat biodiesel in soybean biodiesel and B20 diesel blends using near infrared spectroscopy and synergy interval support vector regression. *Talanta*, **2014**. *119*, 582-589.
50. Dingari, N.C.; Barman, I.; Myakalwar, A.K.; Tewari, S.P.; Gundawar, M.K. Incorporation of support vector machines in the LIBS toolbox for sensitive and robust classification amidst unexpected sample and system variability. *Anal Chem*, **2012**. *84*, 2686-2694.
51. Niazi, A.; Goodarzi, M.; Yazdanipour, A. Comparative study between least-squares support vector machines and partial least squares in simultaneous spectrophotometric determination of cypermethrin, permethrin and tetramethrin. *J Brazil Chem Soc*, **2008**. *19*, 536-542.
52. Kennard, R.W.; Stone, L.A. Computer aided design of experiments. *Technometrics*, **1969**. *11*, 137-148.
53. Berrar, D., *Cross-validation*, in *Encyclopedia of Bioinformatics and Computational Biology*, S. Ranganathan, et al., eds. 2019, Academic Press: Oxford. p. 542-545.

54. Shao, Z.; Er, M.J. Efficient Leave-one-out cross-validation-based regularized extreme learning machine. *Neurocomputing*, **2016**. *194*, 260-270.
55. Wong, T.-T. Performance evaluation of classification algorithms by k-fold and leave-one-out cross validation. *Pattern Recognition*, **2015**. *48*, 2839-2846.
56. Box, G.E.P. Non-normality and tests on variances. *Biometrika*, **1953**. *40*, 318-335.

Tables and Figures

Table 1. Performance comparison results between the PLS and SVM calibration models.

	Prepared fuel-blend volume fraction		Total specific energy release (heating value)	
	PLS	SVM	PLS	SVM
RMSEC ^a	15.65 %	5.49 %	0.85 kJ g ⁻¹	0.47 kJ g ⁻¹
RMSECV ^b	21.01	10.74	1.12	0.91
RMSEP ^c	14.70 %	8.09 %	0.62 kJ g ⁻¹	0.49 kJ g ⁻¹
Rcal ^d	0.87	0.98	0.85	0.96
Rval ^e	0.88	0.98	0.89	0.94
LVs ^f	5	-	5	-

^aroot mean square error of calibration.

^broot mean square error of cross-validation.

^croot mean square error of validation.

^dPearson's correlation coefficient between real and predicted property (calibration).

^ePearson's correlation coefficient between real and predicted property (validation).

^fnumber of latent variables.

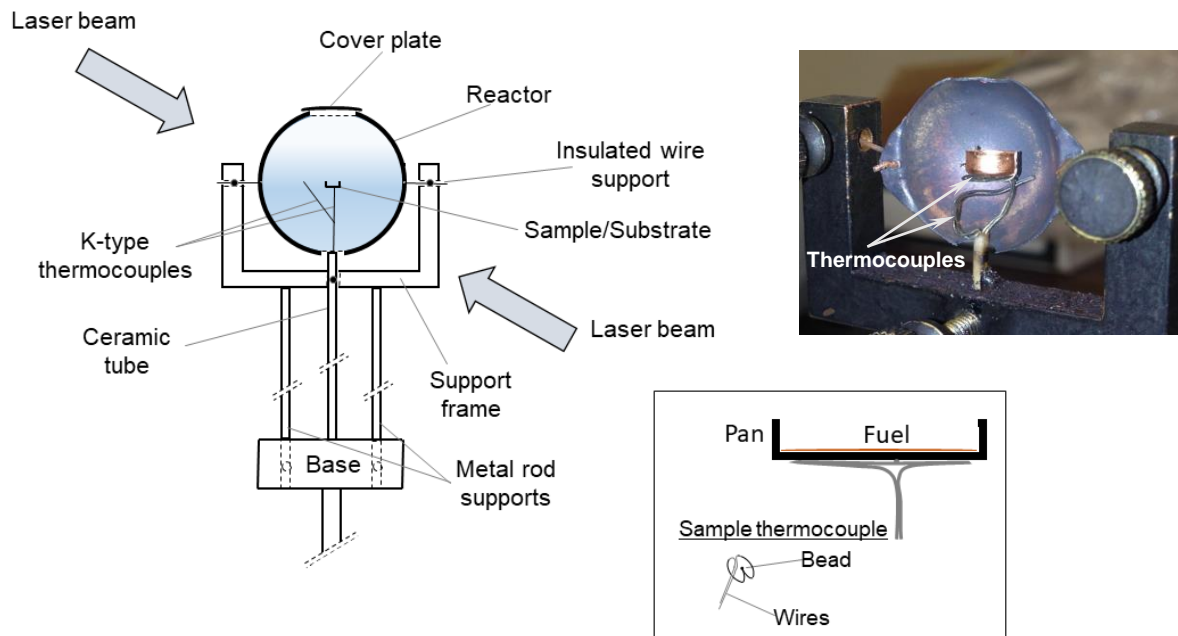


Figure 1. Schematic and photograph of the reactor sphere. Insert illustrates the shape of the sample thermocouple, which also supports the copper pan substrate.

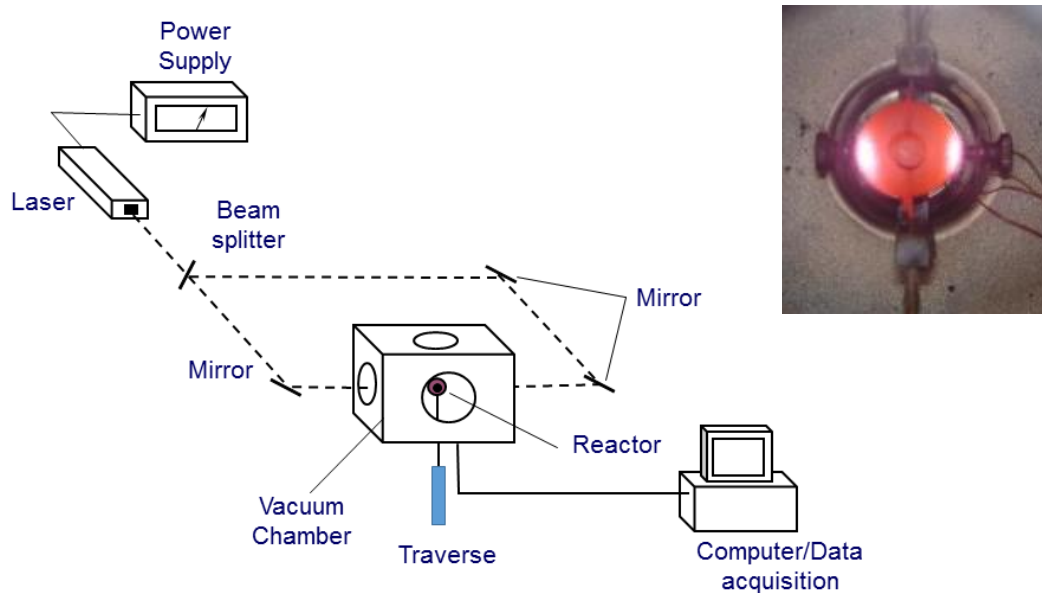


Figure 2. Schematic of the experimental arrangement. Insert is a photograph of the reactor sphere being heated by the laser beam.

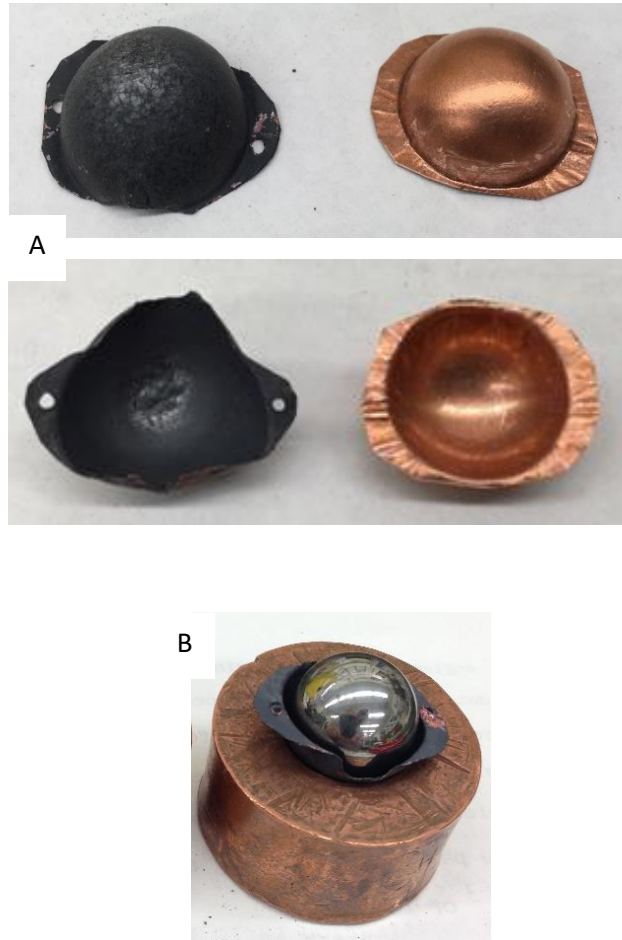


Figure 3. Photograph of a used and newly prepared copper hemisphere: A) comparison of the used-sphere surface to that of the new sphere, and B) expansion of the used-sphere diameter compared to the original diameter. The steel ball shown in this image was used as a form to create the copper sphere.

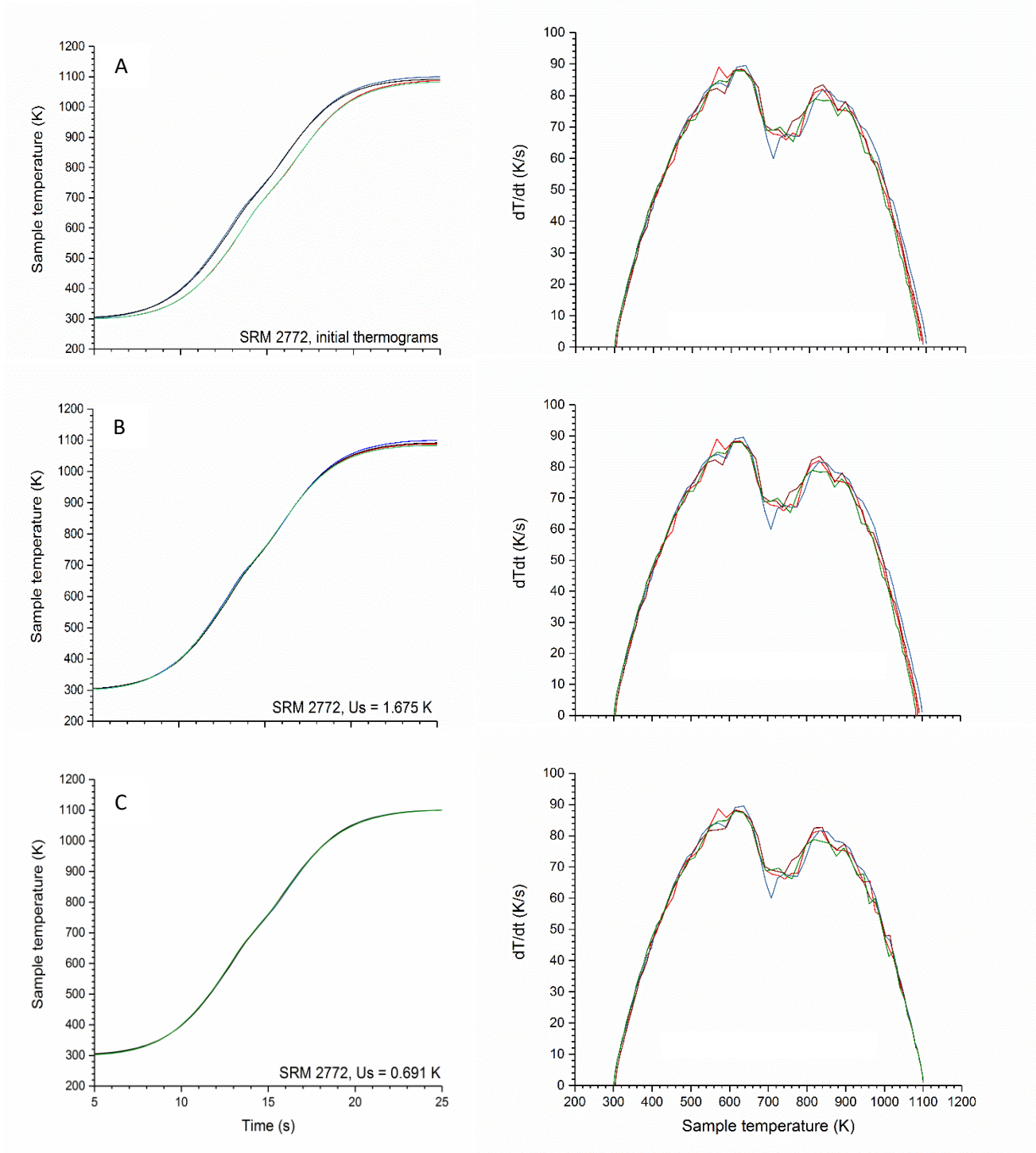


Figure 4. Translation and extrapolation of the data set for SRM 2772: A) initial thermogram measurements, B) translated curves in time, and C) extrapolated curves to the highest steady-state temperature.

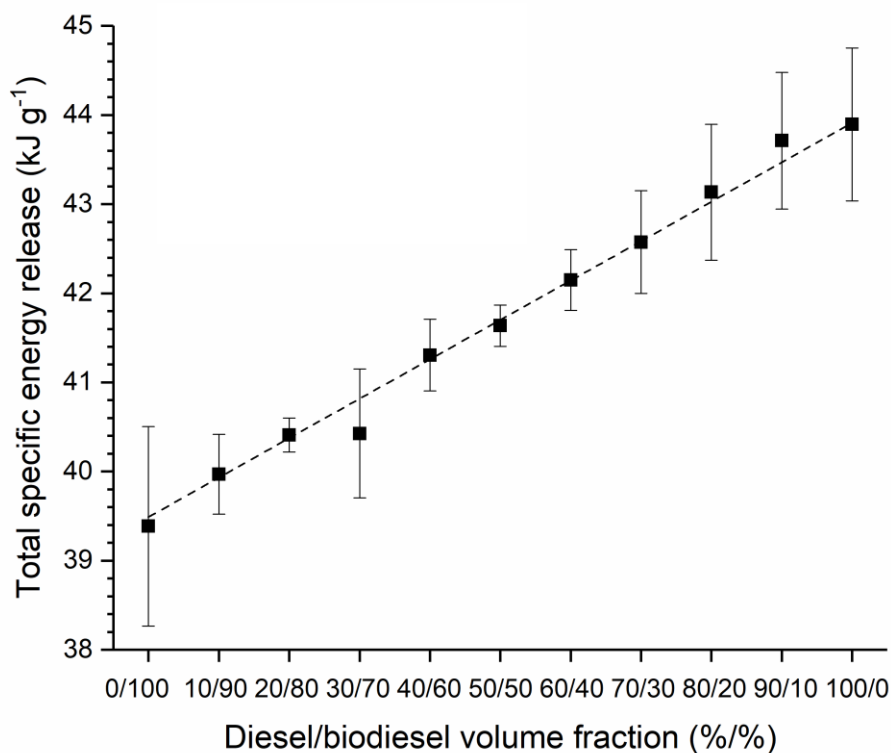


Figure 5. Variation of the total specific energy release (heating value) with prepared fuel-blend volume fraction (average of the four replicated thermograms) using the sphere analysis. The volume fraction 0/100 % refers to SRM 2772 (biodiesel) and 100 %/0 refers to SRM 2770. The error bars represent the expanded uncertainty (95 % confidence level). The linear fit through the data is represented by: $y = a + bx$ where $a = 39.49 \pm 0.06$ and $b = 0.044 \pm 0.001$.

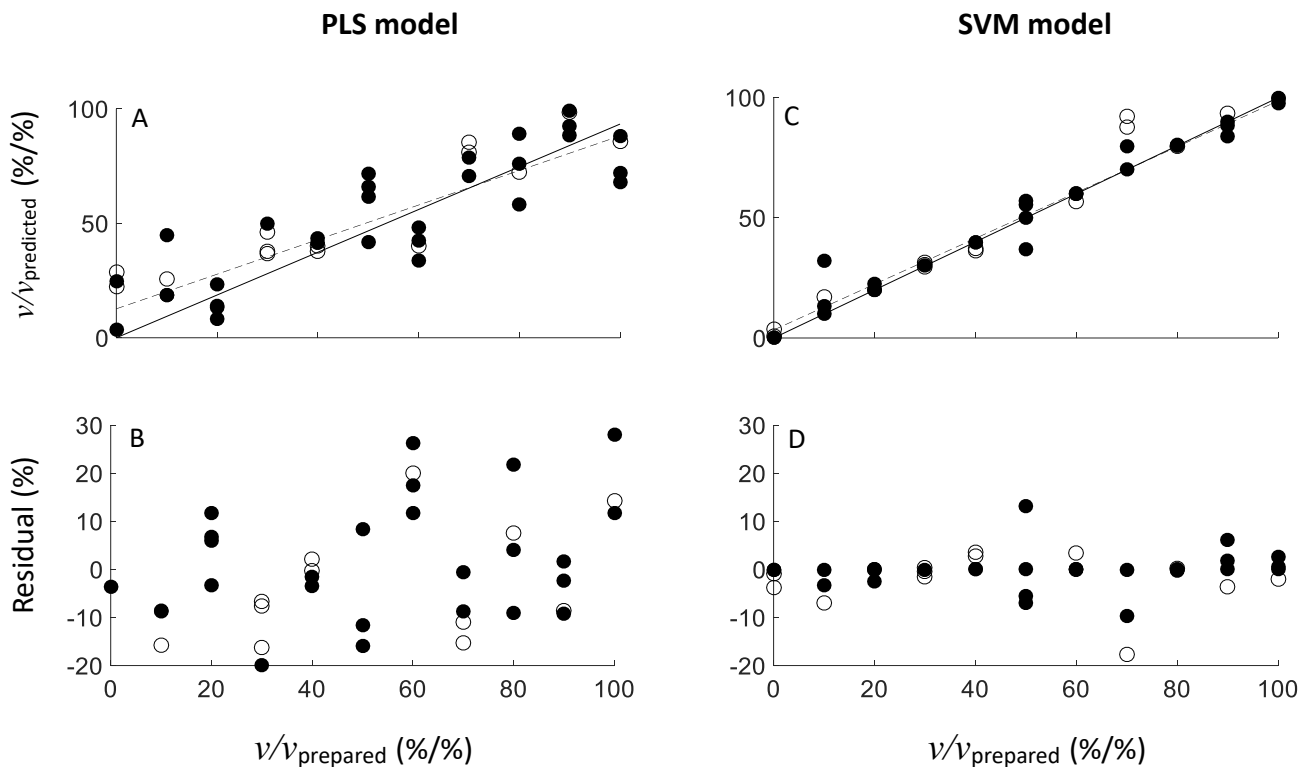


Figure 6. Variation of the model prediction (A,C) and residual (B,D) with prepared fuel-blend volume fraction (v/v) of the diesel/biodiesel fuel blends, using the PLS and SVM models. Closed symbols: calibration samples, open symbols: validation samples. Dashed line: linear fit to calibration data, solid line: $y = x$ calibration line.

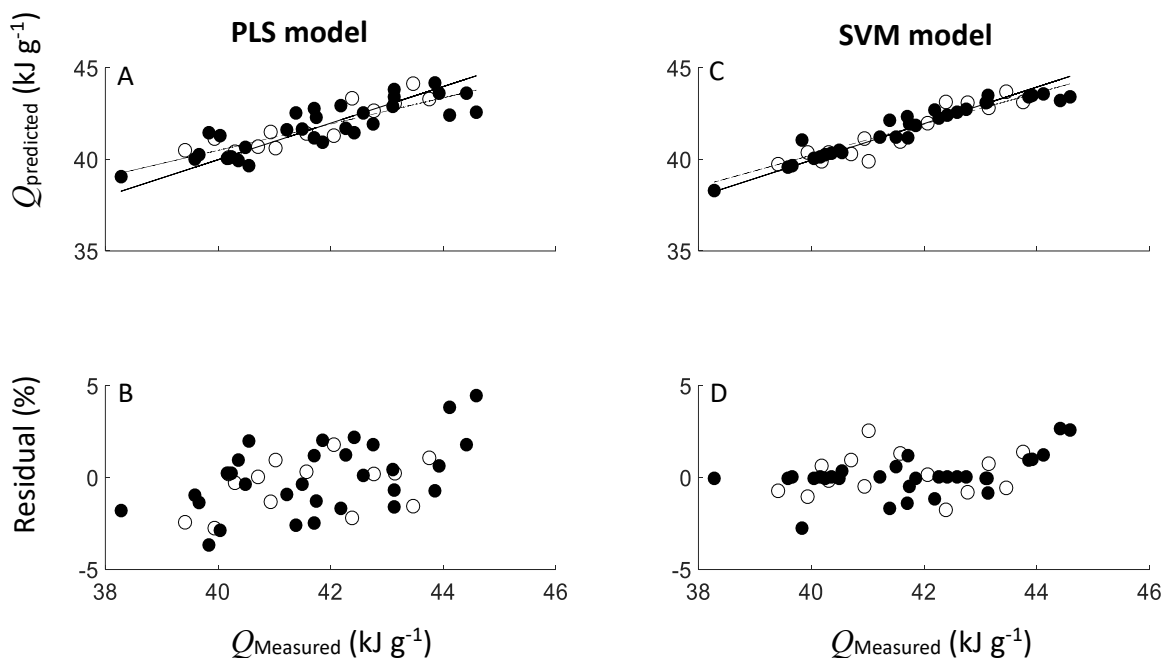


Figure 7. Variation of the model prediction (A,C) and residual (B,D) with measured total specific energy release (Q) of the diesel/biodiesel fuel blends, using the PLS and SVM models. Symbols and lines are the same as in Fig. 6.

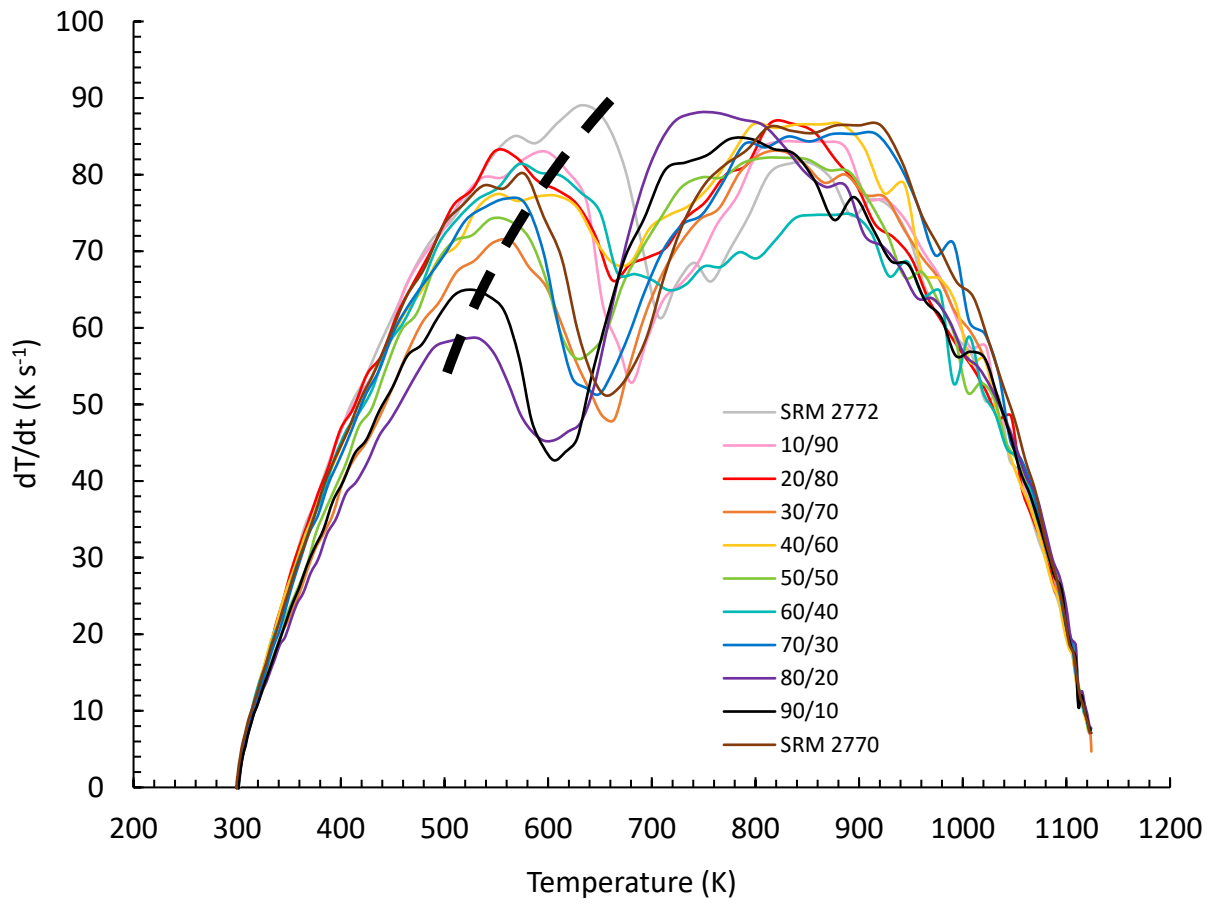


Figure 8. Variation of the average temperature-time derivative (dT/dt) with sample temperature for all prepared fuel-blend volume fractions.